Three-dimensional forward modeling for the SBTEM method using an unstructured finite-element method*

Wang Lu-Yuan[1], Yin Chang-Chun♦[1], Liu Yun-He[1], Su Yang[1], Ren Xiu-Yan[1], Hui Zhe-Jian[1], Zhang Bo[1], and Xiong Bin[2]

Abstract: In this study, we propose a three-dimensional (3D) forward modeling algorithm of surface-to-borehole transient electromagnetic (SBTEM) fields based on an unstructured vector finite-element method to analyze the characteristics of SBTEM responses for complex geoelectrical models. To solve the double-curl diffusion equation for the electric field, we use an unstructured tetrahedral mesh to discretize the model domain and select the unconditionally stable backward Euler scheme to discretize the time derivative. In our numerical experiments, we use a grounded wire as a transmitting source. After validating the algorithm's effectiveness, we first analyze the diffusion characteristics and detectability of the electromagnetic field. After that, we focus our attention on the distribution and the cause of zero bands for Ex and dBy/dt components with the hope of guiding future field surveys. Finally, by simulating different models, we analyze the capability of the SBTEM method in detecting typical mineral veins so that we can provide a reference for mineral resource exploration in the deep earth.
Keywords: Surface-to-borehole TEM, forward modeling, edge-based FE method, unstructured grids, zero bands

Introduction

With the rapid development of China's economy, the demand for mineral resources is growing rapidly. However, nowadays, the mining depth of mineral resources in China is mainly within 500 m (Di, et al., 2019). How to develop electromagnetic (EM) detection technology for deep resources and to effectively detect mineral resources in the deep earth is an important direction in this EM research.

The transient electromagnetic (TEM) method is a common geophysical exploration technology that has been widely used in mineral exploration (Swidinsky et al., 2012; Oldenburg et al., 2013), water resource investigation (Porsani et al., 2012; Meier et al., 2014), and the study of deep earth structures (Strack et al., 1990; Haroon et al., 2015). The transmitting source and receivers of traditional TEM methods are both deployed at the earth's surface because the resolution is limited due to the distance from the anomalous body, resulting

in poor detectability of deep targets. In contrast, the surface-to-borehole TEM (SBTEM) method can improve the resolution of deep targets because the transmitting source is placed around the borehole, and the receivers are placed in the borehole to observe the EM field (Li, 2015). A decrease in the distance between a receiver and abnormal bodies greatly improves signal quality so that both the signal intensity and resolution of targets can be improved (Augustin et al., 1989). In the early stage, the SBTEM method was used in exploring energy and mineral resources. Dyck and West (1984) proved the superiority of the SBTEM method in detecting good deep conductors based on field study; Macnae and Staltari (1987) analyzed the sign reversal phenomenon of SBTEM responses caused by coupling downhole probe and EM field; Newman et al. (1989) studied the influence of an underground conductor on SBTEM responses by forward modeling and verified the theoretical results through a field test; Spies and Greavesb (1991) numerically simulated the Holt Sand in situ combustion reservoir to enhance oil recovery, proving that the SBTEM method has an advantage of high resolution in recording dynamic reservoirs; Buselli and Lee (1996) simulated SBTEM responses when there is overburden and explained the effect of polarity reversal and peak change in survey data. However, limited by observation conditions at that time, the SBTEM method has not been further used. In recent years, after extensive exploration and development of mineral resources, a large number of drilling holes have been laid in the mining areas. This provides conditions for SBTEM observations. Accordingly, research on the SBTEM method is increasing both at home and abroad. Colombo et al. (2013) verified technical advantages of the SBTEM method in describing anisotropic effects and improving reservoir resolution through water injection monitoring of carbonate reservoirs in Saudi Arabia; Cuevas et al. (2015) conducted on-site testing on SBTEM observation systems and analyzed the impact of the receiver in the borehole via numerical simulation of typical environments; Jiang et al. (2019) proposed a surface-to-underground TEM method based on studies on the SBTEM method and verified the detectability of the method to detect deep water-filled goaf through comprehensive data inversion and field application; Chen et al. (2019) analyzed the detectability of SBTEM fields based on one-dimensional (1D) simulations.

Three-dimensional (3D) numerical modeling of the SBTEM method mainly includes the integral equation (IE) method (West and Ward, 1988; Li and He, 2012; Li, et al., 2017), the finite- difference (FD) method (Eaton

and Hohmann, 1984; Meng and Pan, 2012; Yang, et al., 2016), and the finite-element (FE) method (Li et al., 2015; Liu et al., 2020). Among them, the IE method has difficulty in accurately simulating complex geological bodies or models with a large electrical difference. The FD method may not be able to deliver accurate results for complex models if no fine grids are implemented. In this study, we choose the FE method based on unstructured grids to calculate the TEM field directly in the time domain. These unstructured grids can perform fine subdivision and accurate simulation of complex underground structures (Ansari and Farquharson, 2014), and a direct solution in the time domain avoids the numerical accuracy problem limiting the traditional frequency-time transformation.

Due to the late emergence of the SBTEM method, analysis and research on its physical mechanism are mainly based on 1D models. Chen et al. (2019) studied the EM diffusion and detectability of a ground wire transmitting source based on a layered earth model and found that Ex and dBy/dt are affected by the return current, and there exist areas with an extremely small field. In this study, we select the ground wire as a transmitting source for a large exploration depth (Xue et al., 2013). For models with terrain or complex underground abnormal bodies, we use the unstructured FE method to calculate SBTEM responses and then studied the zero band distribution characteristics of TEM fields in the borehole. We also discuss the characteristics of SBTEM responses for typical 3D underground anomalous bodies.

In a sequence, we first introduce 3D forward modeling technology for the SBTEM method based on unstructured grids. After verifying our algorithm's accuracy, we study the diffusion of SBTEM fields of Ex and dBy/dt and zero bands. Finally, we explore the response characteristics of the SBTEM method and the detection capability of the method in detecting different abnormal bodies.

Forward modeling

Governing equations

Maxwell's equations for time domain EM can be written as

$$\nabla \times \mathbf{E}(\mathbf{r},t) = -\mu \frac{\partial \mathbf{H}(\mathbf{r},t)}{\partial t}, \tag{1}$$

$$\nabla \times \mathbf{H}(\mathbf{r},t) = \sigma \mathbf{E}(\mathbf{r},t) + \varepsilon \frac{\partial \mathbf{E}(\mathbf{r},t)}{\partial t} + \mathbf{j}_s(\mathbf{r},t), \tag{2}$$

where $\mathbf{E}(\mathbf{r},t)$ and $\mathbf{H}(\mathbf{r},t)$ are the electric and magnetic fields, respectively. μ represents the magnetic permeability, ε represents the dielectric permittivity, σ represents the conductivity, and $\mathbf{j}_s(\mathbf{r},t)$ is the source current. From equations. (1) and (2), we can obtain the full-wave equation for the electric field (Um, 2011), i.e.,

$$\nabla \times \left[\frac{1}{\mu_0} \nabla \times \mathbf{E}(\mathbf{r},t) \right] + \varepsilon_0 \frac{\partial^2 \mathbf{E}(\mathbf{r},t)}{\partial t^2} + \sigma \frac{\partial \mathbf{E}(\mathbf{r},t)}{\partial t} + \frac{\partial \mathbf{j}_s(\mathbf{r},t)}{\partial t} = 0. \tag{3}$$

Space discretization for FE method

We use the open-source code TetGen (Si, 2007) to divide the model domain into tetrahedral meshes and use the Galerkin method to discretize equation (3). For that purpose, we expand the electric field in the eth element (Jin, 1998) as

$$\mathbf{E}^{\mathrm{e}}(\mathbf{r},t) = \sum_{j=1}^{n} \mathbf{E}_j^e(\mathbf{r},t) = \sum_{j=1}^{n} u_j^e(t) \mathbf{n}_j^e(\mathbf{r}), \tag{4}$$

where $u_j^e(t)$ denotes the unknown electric field at edge j of element e, whereas $\mathbf{n}_j^e(\mathbf{r})$ is the edge-based functions at edge j of element e. The residual vector is defined as

$$\mathbf{p}^{\mathrm{e}}(\mathbf{r},t) = \frac{1}{\mu_0} \nabla \times \nabla \times \mathbf{E}(\mathbf{r},t) + \varepsilon_0 \frac{\partial^2 \mathbf{E}(\mathbf{r},t)}{\partial t^2}$$
$$+ \sigma \frac{\partial \mathbf{E}(\mathbf{r},t)}{\partial t} + \frac{\partial \mathbf{j}_s(\mathbf{r},t)}{\partial t}. \tag{5}$$

According to the Galerkin method, we choose the edge-based functions $\mathbf{n}_j^e(\mathbf{r})$ as the weighting function to perform residual weighting and integration, so we can obtain

$$\iiint_{V^e} \mathbf{n}_j^{\mathrm{e}}(\mathbf{r}) \cdot \mathbf{p}^{\mathrm{e}}(\mathbf{r},t) dV = 0. \tag{6}$$

From equation (6), we can finally obtain the FE equation for the electric field, (Um, 2011) i.e.,

$$\mathbf{A}^{\mathrm{e}} \frac{d^2 \mathbf{u}^e(\mathbf{r},t)}{dt^2} + \mathbf{B}^{\mathrm{e}} \frac{d \mathbf{u}^e(\mathbf{r},t)}{dt} + \mathbf{C}^e \mathbf{u}^e(t) + \mathbf{s}^e = 0, \tag{7}$$

where the elements of the dielectric constant matrix, conductivity matrix, and permeability matrix are, respectively, given by

$$A_{ij}^{\mathrm{e}} = \iiint_{V^e} \varepsilon^{\mathrm{e}} \mathbf{n}_i^{\mathrm{e}}(\mathbf{r}) \cdot \mathbf{n}_j^{\mathrm{e}}(\mathbf{r}) dV, \tag{8}$$

$$B_{ij}^{\mathrm{e}} = \iiint_{V^e} \sigma^{\mathrm{e}} \mathbf{n}_i^{\mathrm{e}}(\mathbf{r}) \cdot \mathbf{n}_j^{\mathrm{e}}(\mathbf{r}) dV, \tag{9}$$

$$C_{ij}^{\mathrm{e}} = \iiint_{V^e} \nabla \times \mathbf{n}_i^{\mathrm{e}}(\mathbf{r}) \cdot \nabla \times \mathbf{n}_j^{\mathrm{e}}(\mathbf{r}) dV, \tag{10}$$

The ith element of the source vector is

$$s_i^{\mathrm{e}} = \iiint_{V^e} \mathbf{n}_i^{\mathrm{e}}(\mathbf{r}) \cdot \frac{\partial \mathbf{j}_s(\mathbf{r},t)}{\partial t} dV. \tag{11}$$

In equation (7), the unknown vector $\mathbf{u}^{\mathrm{e}} = \left[u_1^e, u_2^e, ..., u_n^e \right]$ represents the electric field at the edges of each element. Neglecting the displacement current, we obtain the following simplified diffusion equations for the electric field:

$$\mathbf{B} \frac{d\mathbf{u}(t)}{dt} + \mathbf{C}\mathbf{u}(t) + \mathbf{s} = 0. \tag{12}$$

Time discretization

To solve equation (12), we need to discretize the partial derivative term with respect to time. In this study, we assume a step wave as the transmitting wave. Due to the huge conductivity difference between air and the underground, if we choose explicit time discretization, the time step needs to be sufficiently small to meet stability conditions, which is very challenging, especially for calculating late time responses. Thus, we choose the unconditionally stable backward Euler (BE) scheme to discretize time. Applying the first-order BE method to equation (12), we obtain

$$\mathbf{u}^{n+1} = \mathbf{u}^n + \Delta t f\left(\mathbf{u}^{n+1}, t_{n+1}\right) \tag{13}$$

where $f\left(\mathbf{u}^{n+1}, t_{n+1}\right) = \frac{d\mathbf{u}}{dt}\Big|_{(t_{n+1}, \mathbf{u}^{n+1})}$. From equation (12), we have

$$\frac{d\mathbf{u}}{dt}\Big|_{(t_{n+1}, \mathbf{u}^{n+1})} = -\frac{1}{\mathbf{B}}\left(\mathbf{C}\mathbf{u}^{n+1} + \mathbf{s}^{n+1}\right), \tag{14}$$

Inserting equation (14) into equation (13), we obtain

$$\mathbf{D}\mathbf{u}^{n+1} = \mathbf{B}\mathbf{u}^n - \Delta t \mathbf{s}^{n+1}, \tag{15}$$

103

where $\mathbf{D}=(\mathbf{B}+\Delta t\mathbf{C})$. Equation (15) provides a recurrence formulation for calculating SBTEM responses.

Boundary and initial conditions

We need to impose the boundary and initial conditions to obtain a unique solution to our forward problem. Here, we choose the homogeneous Dirichlet boundary conditions by setting the electric field to zero on the outer boundary. For the step-off source, following Um (2011), the initial electric field can be divided into two parts, source electric and direct current (DC) fields, i.e.,

$$\mathbf{E}_{\text{initial}} = \mathbf{E}_{\text{source}} + \mathbf{E}_{\text{DC}}, \qquad (16)$$

where $\mathbf{E}_{\text{initial}}$ is the initial electric field, $\mathbf{E}_{\text{source}}$ is the source electric field, and $\mathbf{E}_{\text{DC}}$ is the DC electric field. The source electric field can be determined through Ohm's law, where the electrical current will be divided into each neighboring element containing electrical current based on the following weight coefficient (Yin, 2016):

$$p_i = \frac{\sigma_i V_i}{\sum_j \sigma_i V_i}, \qquad (17)$$

where σ_i and V_i represent the conductivity and volume of the ith element, respectively. To calculate the DC electric field, we need to solve a 3D Poisson equation for electrical potential (Hui et al., 2020), i.e.,

$$\nabla \cdot (\sigma\varphi(\mathbf{r})) = -\nabla \cdot \mathbf{j}_s(\mathbf{r}) \qquad (18)$$

After solving the electric potential, we can use the derivative relationship between the node electric potential and the edge DC electric field to calculate $\mathbf{E}_{\text{DC}}$.

Numerical experiments

Since we choose a long ground wire along the

x-direction as the transmitting source in this study, the electric component Ey is small. Besides, in the three components of the magnetic field, only dBy/dt has a strong signal, whereas the signals of dBx/dt and dBz/dt are poor. Thus, we choose Ex, Ez, and dBy/dt for our simulation and response analysis.

Accuracy verification

To validate our modeling algorithm, we choose a homogenous half-space model in Figure 1 and compare our 3D forward results with 1D semi-analytical solutions. The transmitting source is 2000-m long, aligned in the x-direction, with the center located at (0 m, 0 m, 0 m). The transmitting current is 1 A. Air resistivity is assumed to be 1×10^8 $\Omega\cdot$m, whereas underground resistivity is 100 $\Omega\cdot$m. Note that for simplicity, we use resistivity instead of conductivity in our subsequent model studies.
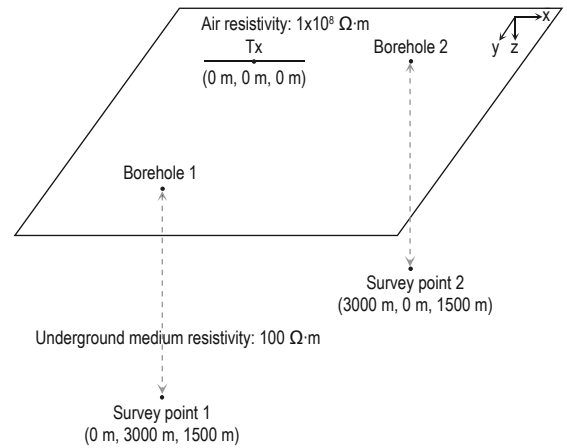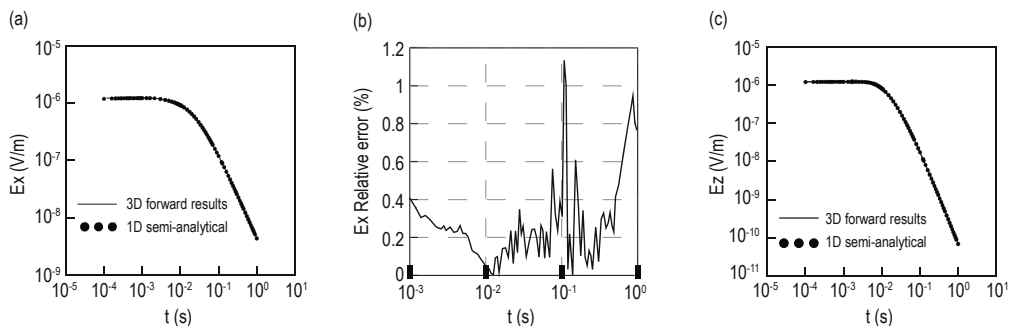

Fig. 1. A homogenous half-space model.

Considering that there exist weak components for the electrical transmitting source, we select Ex, dBy/dt, and dBz/dt components at survey point 1 and Ex, Ez, dBy/dt at survey point 2 for our accuracy evaluation.
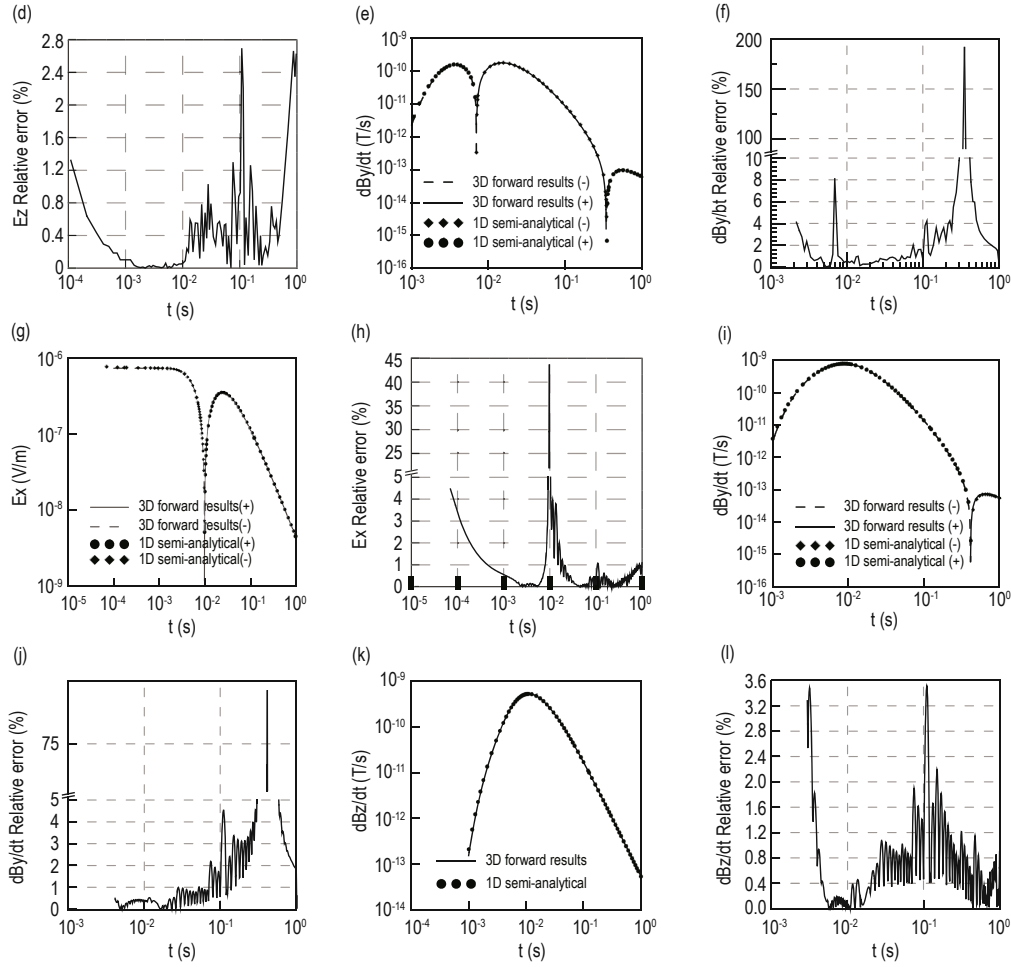
Fig. 2. Comparison of a homogeneous half-space model's accuracy with that of semi-analytical solutions.
(a) Ex, (b) relative error for Ex, (c) Ez, (d) relative error for Ez, (e) dBy/dt, (f) relative error for dBy/dt, (g) Ex, (h) relative error for Ex, (i) dBy/dt, (j) relative error for dBy/dt, (k) dBz/dt, and (l) relative error for dBz/dt. (a)–(f) are responses for survey point 2, and (g)–(l) are responses for survey point 1. The dashed lines denote negative responses.

Figure 2 shows the comparison of our modeling results with the semi-analytical solutions. It is seen that the relative errors of Ez and dBz/dt are less than 5%. The relative errors of Ex and dBy/dt are less than 5% at most times. Only when the EM field changes signs does the error become significant. Thus, we can confirm the high accuracy of our 3D forward modeling algorithm. In addition, a comparison of Figures 2a and 2g with Figures 2b and 2h shows that the time with large relative errors of Ex corresponds to the zero band of |Ex|. Besides, the zero band of |Ex| only appears at survey point 1, and no zero band is observed at survey point 2. Meanwhile, the comparison of Figures 2e and 2i with Figures 2f and 2j shows that the time with a large relative error for dBy/dt corresponds to the zero band of |dBy/dt| as well. We will discuss the sign reversal issue in the next section.

Zero band of Ex and dBy/dt

To study zero band characteristics, we calculate Ex and dBy/dt responses in a homogeneous half-space (refer to Figure 1 for model information). The transmitting source is 2000-m long, aligned in the x-direction, with the center located at (0 m, 0 m, 0 m). The transmitting current is 1 A. Air resistivity is assumed to be 1×10^8 $\Omega \cdot m$, and underground resistivity is assumed to be 1, 10, and 100 $\Omega \cdot m$, respectively. Figures 3 and 4 are the cross-sections of Ex and dBy/dt for the half-space model at y = 0, 1000, 2000, 3000, and 4000 m, respectively. The figures show that there exist obvious zero bands of Ex and dBy/dt. The zero band is mainly caused by the current distribution of the electrical transmitting source. After the current is turned off, the decaying current and the "return current" due to impedance (Gunderson

105

et al., 1986; Chen et al., 2019) will form a clockwise vortex directly below the transmitting source, changing the direction of the electric field in the center of the

vortex. This leads to the zero band of Ex. Meanwhile, the horizontal magnetic field in the vortex area points in the negative y-axis direction, whereas the horizontal
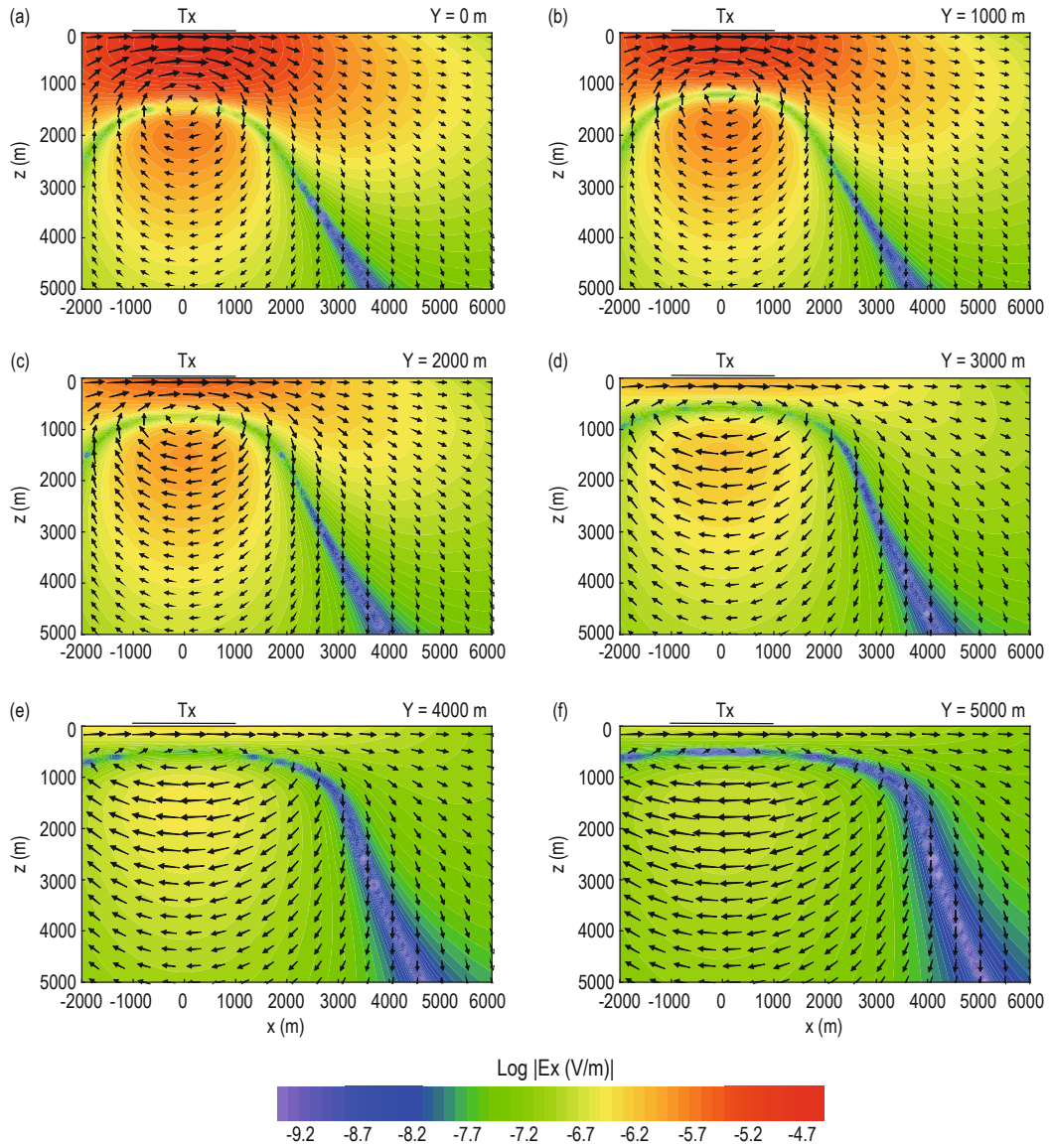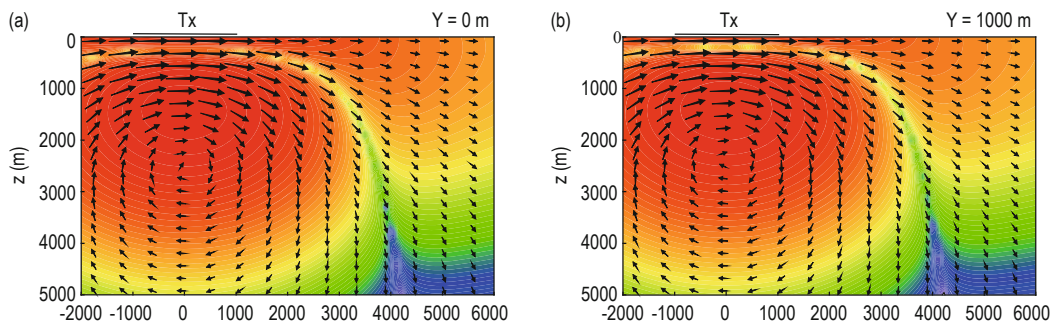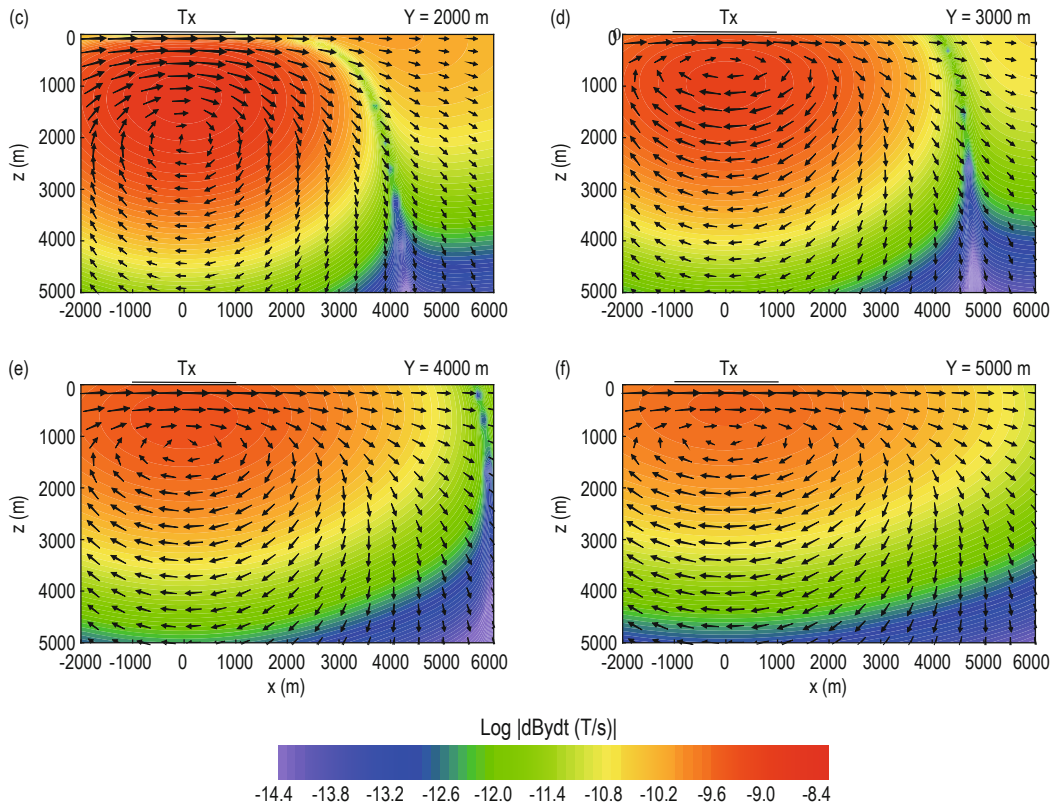

Fig. 3. Distribution of current and horizontal electric field Ex in a homogeneous half-space (t = 3 ms).
(a) y = 0 m, (b) y = 1000 m, (c) y = 2000 m, (d) y = 3000 m, (e) y = 4000 m, and (f) y = 5000 m.

Fig. 4. Distribution of current and horizontal magnetic field dBy/dt in a homogeneous half-space (t = 3 ms). (a) y = 0 m, (b) y = 1000 m, (c) y = 2000 m, (d) y = 3000 m, (e) y = 4000 m, and (f) y = 5000 m.

magnetic field in the area away from the current source points in the positive y-axis direction. As a result, a dBy/dt zero band is formed at the junction of the two regions. Analyzing the current direction on the side profile in Figures 3 and 4, as the side profiles gradually move away from the transmitting source, the zero bands of Ex and dBy/dt move gradually upward and outward, demonstrating EM diffusion characteristics.

To analyze the EM diffusion characteristics and zero bands of Ex and dBy/dt, we display in Figures 5 and 6, the time-varying characteristics of EM fields in a homogenous half-space of varying resistivities. The figures show that the EM field propagates outward and downward, decaying with time. The larger the half-space resistivity, the faster the EM diffusion and attenuation. The position of the zero band of Ex gradually moves downward with time, whereas the position of the zero band of dBy/dt gradually moves outward, but the overall shape remains unchanged. The higher the half-space resistivity, the faster the zero bands move. Further comparison shows that as the zero band of Ex moves downward with time, the influence on EM detection mainly occurs at the early stage, with almost no influence observed at the late stage. However, the dBy/dt zero band moves outward over time, which will have an impact on the entire time.
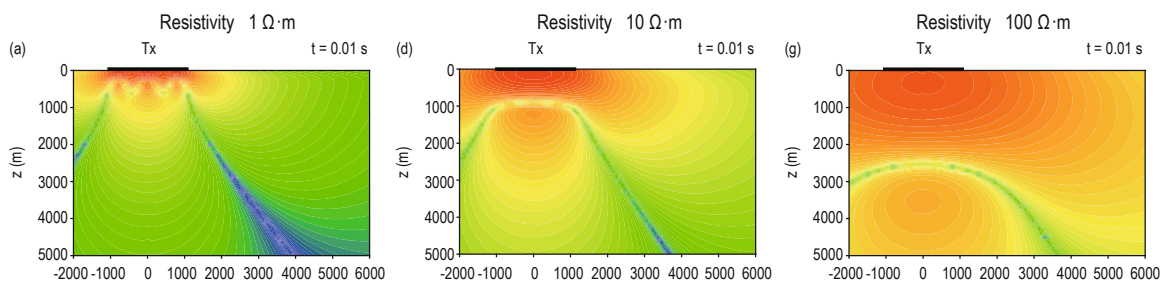
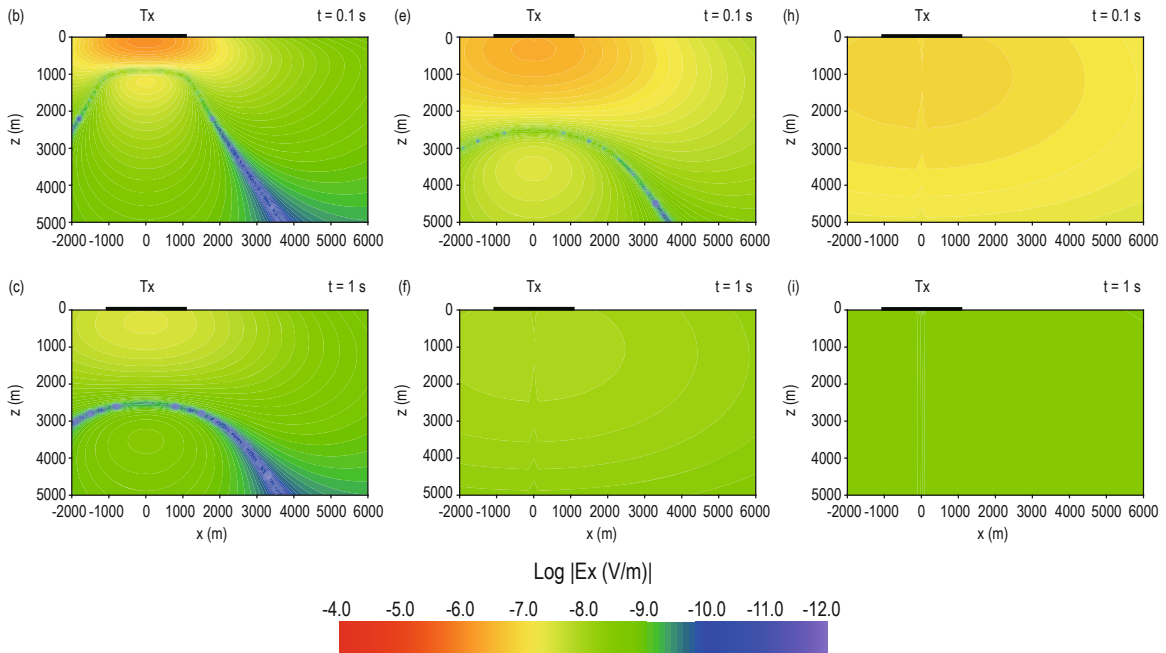# Three-dimensional forward modeling for the SBTEM

Fig. 5. Diffusion of Ex in a homogeneous half-space of varying resistivities (y = 0).
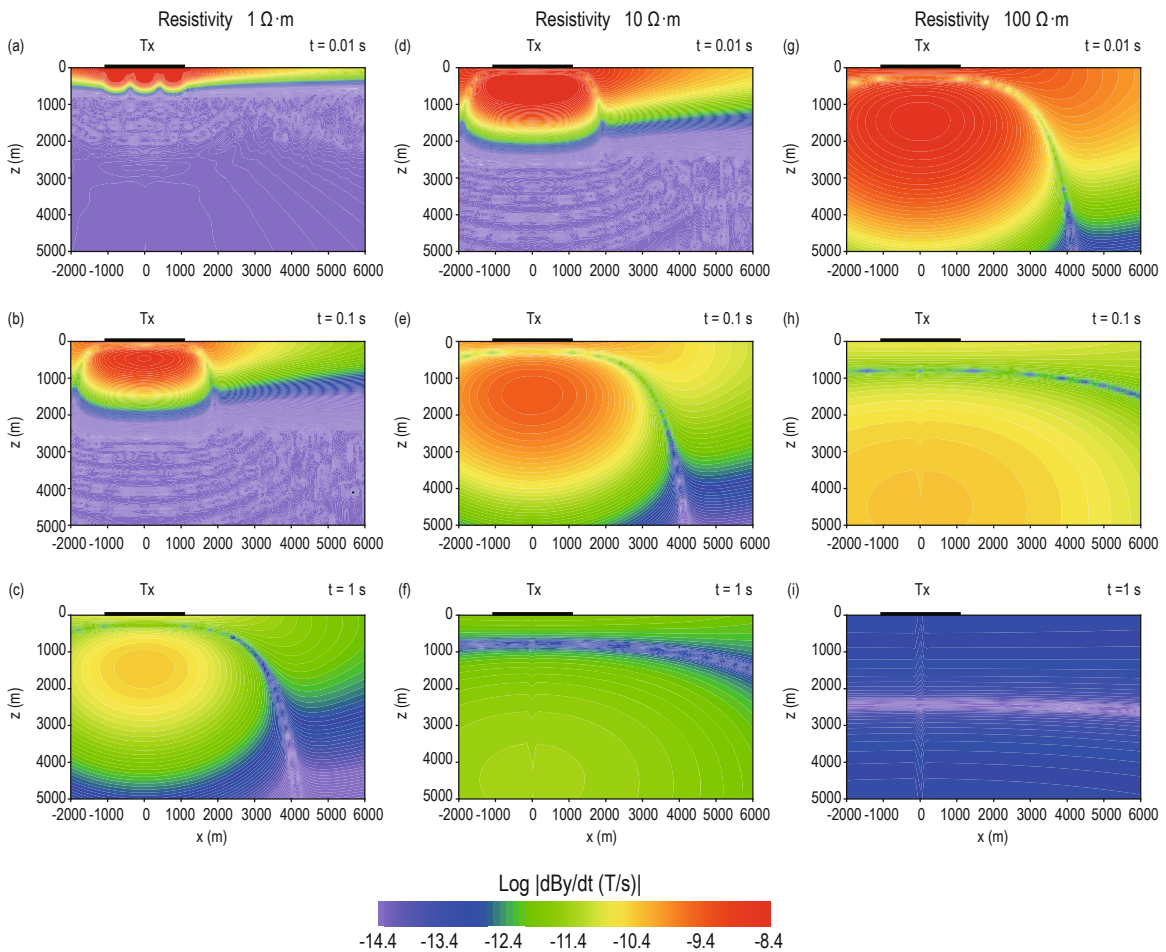(a), (d), and (g) are for t = 0.01 s; (b), (e), and (h) are for t = 0.1 s; (c), (f), and (i) are for t = 1 s.

Fig. 6. Diffusion of dBy/dt in a homogeneous half-space of varying resistivities (y = 0).
(a, (d), and (g) are for t = 0.01 s; (b), (e), and (h) are for t = 0.1 s; (c), (f), and (i) are for t = 1 s.

EM responses for 3D anomalous bodies

In this section, we design a 3D anomalous body embedded in a homogenous half-space and simulate the diffusion of EM fields measured in line. As shown in Figure 7, the transmitting source Tx is 2000-m long, aligned in the x-direction with the center located at (0 m, 0 m, 0 m). The transmitting current is 1 A. Air resistivity
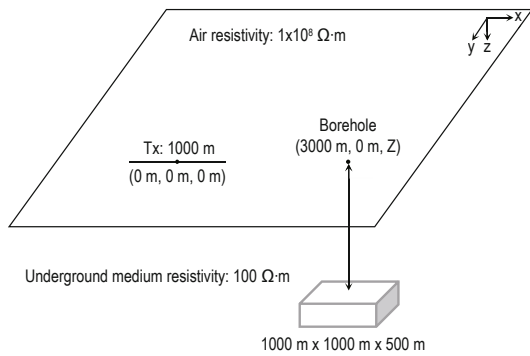
is assumed to be 1×10^8 Ω·m, and the background resistivity is 100 Ω·m. The anomalous body has a resistivity of 10 Ω·m and a central depth of 2000 m.

Figure 8 shows the diffusion of Ex, Ez, and dBy/dt on the main profile (y = 0). The EM fields diffuse downward and outward over time, the amplitude attenuates, showing the diffusion characteristics of EM induction. At the early time [Figures 8a–8c], the EM fields have not yet reached the abnormal body, and little influence can be seen from it. As time passes [Figures 8d–8f], the EM fields pass through the low-resistivity abnormal body and a current channeling occurs, so we can see the concentration of EM fields toward the abnormal body and obvious EM anomaly zones in these areas. At the later time [Figures 8g–8i], the EM fields become completely concentrated on the abnormal body.

In addition, Figures 8c, 8f, 8i, and 8l show that with time passing, the zero band of dBy/dt gradually approaches the abnormal body, and the distribution of
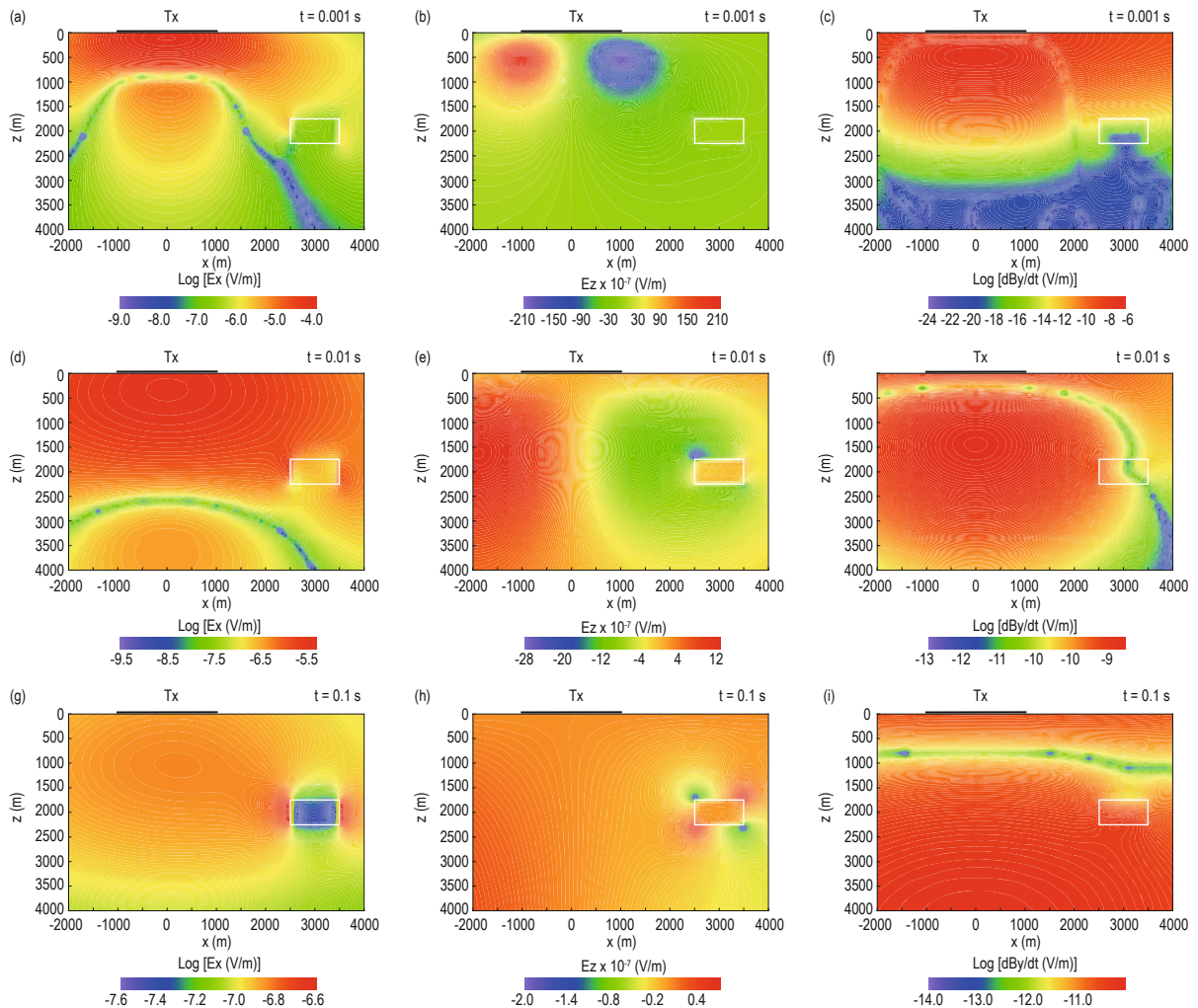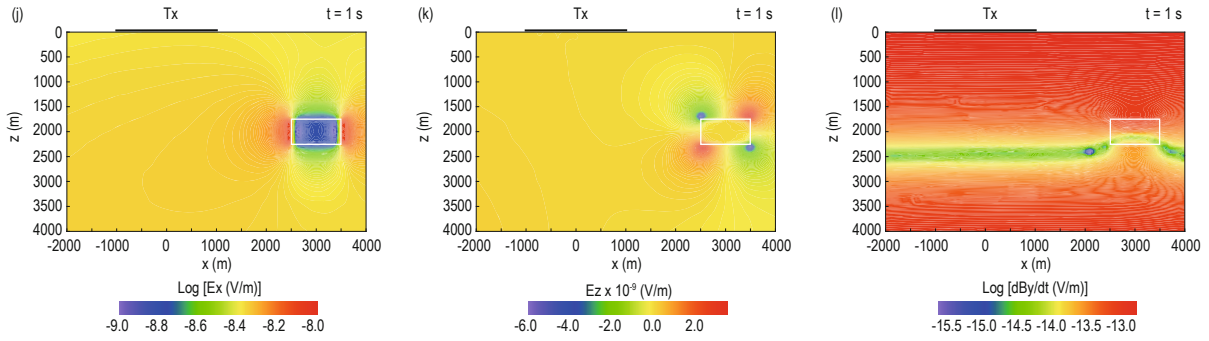

Fig. 7. A 3D body embedded in a homogeneous half-space.

Fig. 8. EM diffusion for a low-resistivity anomalous body embedded in a homogeneous half-space (y = 0). (a)–(c) t = 0.001s, (d)–(f) t = 0.01s, (g)–(i) t = 0.1s, (j)–(l) t = 1s.(a), (d), (g), and (j) are for Ex; (b), (e), (h), and (k) are for Ez; (c), (f), (i), and (l) are for dBy/dt.

the EM field is severely distorted. Comparing Figures 8a, 8d, 8g, and 8j, due to the fast downward movement of the Ex zero band, no effect can be seen on the distribution of the EM field around the anomaly body at the late time.

To further study the response characteristics of complex abnormal bodies in the SBTEM method, we design a dyke model shown in Figure 9. The transmitting source is 2000-m long, aligned in the x-direction, with its center located at (1500 m, 0 m, 0 m). The transmitting current is 1 A. Air resistivity is assumed to be 1×10^8 Ω·m, and background is 100 Ω·m, whereas the resistivity of the anomalous body is 2 Ω·m, with its center located at 2000-m deep. Figure 10 shows the distributions of Ex, Ez, and dBy/dt at the main profile (y = 0). The figure shows that there exists a clear correlation between underground abnormal EM responses and the dyke,

the shape of the dyke is observed. This implies that the SBTEM method can effectively detect deep conductive targets.
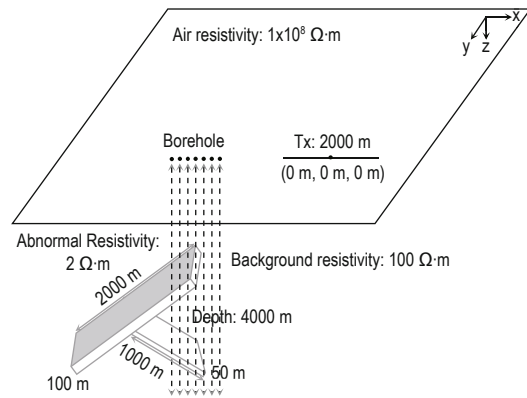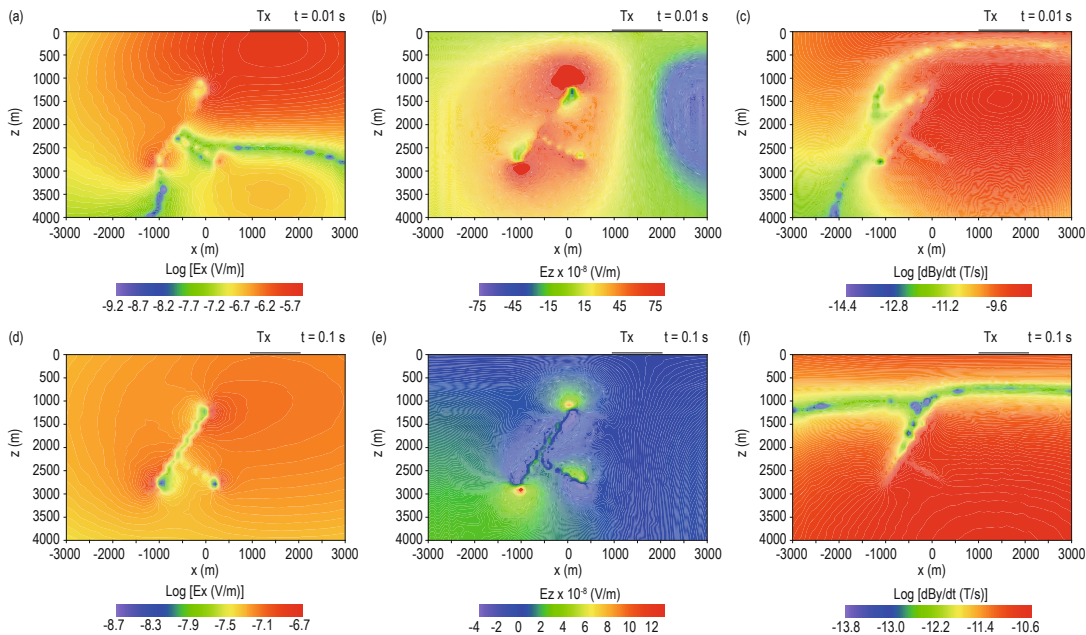

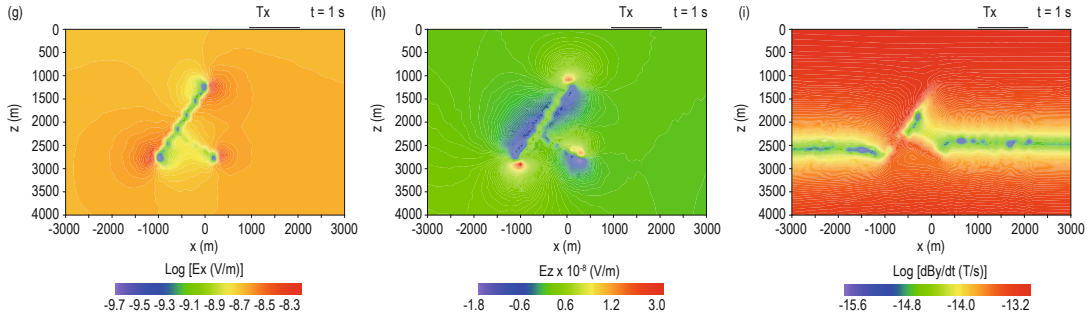**Fig. 9. Two conductive dykes embedded in a homogeneous half-space.**

Fig. 10. EM field distribution for the dyke model in Figure 7.
(a)–(c) t = 0.01s, (d)–(f) t = 0.1s, and (g)–(i) t = 1s. (a), (d), and (g) are for Ex; (b), (e), and
(h) are for Ez, while (c) (f) (i) are for dBy/dt.

Considering the limited number of actual drilling holes, the calculation results in this study can provide a theoretical basis for designing the best borehole positions and observation methods. Concretely, according to the simulation results in Figure 10, we can choose the location with the most obvious anomaly to lay the borehole. Figure 11 shows the curves of EM responses for three components of Ex, Ez, and dBy/dt in the borehole. We assume that the boreholes are aligned in the x-direction with a spacing of 100 m, and in each borehole, we assume 41 survey points at an interval of 100 m. Figure 11 shows that the EM responses in the borehole passing through the abnormal body and the boreholes within 200 m from the abnormal body have obvious anomalies, with the top and bottom of the abnormal body being distinguished. However, as the distance from the abnormal body increases, the anomalies gradually weaken. Since the transmitting source is located at the earth's surface, the anomaly of the deep target is weak, so the resolution of the target becomes worse with an increase in the depth.
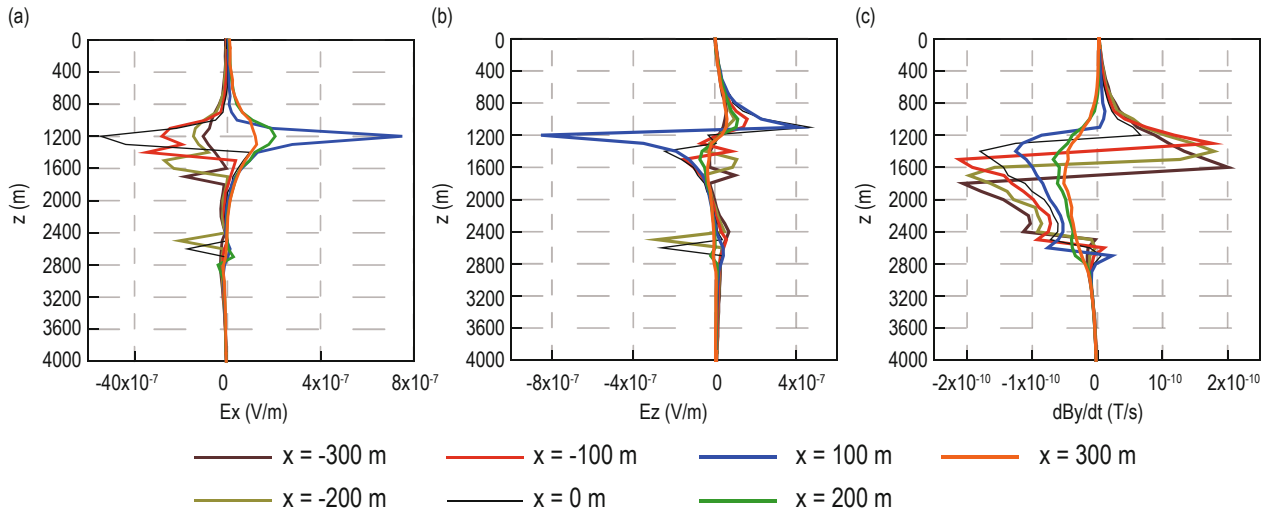

Fig. 11. EM responses for the dyke model in Figure 7 (t = 0.015 s).
(a) Ex, (b) Ez, and (c) dBy/dt.

To better demonstrate the ability of the unstructured FE method presented in this study for simulating complex underground structures and explore the superiority of the SBTEM method in detecting deep conductors under complex terrain, we design in this section an undulating terrain model with a low-resistivity plate embedded (Figure 12). The transmitting source is 2000-m long, aligned in the x-direction with the center located at (-500 m, 600 m, 0 m). The transmitting current is 1 A. Air resistivity is assumed to be 1×10^8 $\Omega \cdot$m, the background resistivity is 100 $\Omega \cdot$m, and the resistivity of the anomalous body is 2 $\Omega \cdot$m, with the center located at 300-m deep. Because of the influence of undulating terrain, it is difficult to distinguish the existence of the

abnormal body from the ground TEM method. As shown in Figure 13, the ground TEM responses for the model are almost the same as the background responses.

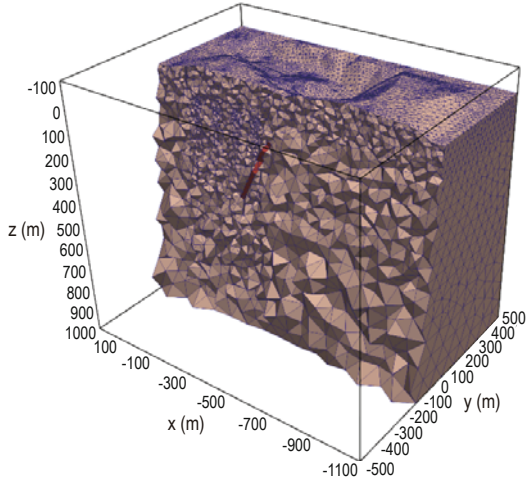The SBTEM method has a better vertical resolution

Fig. 12. A low-resistivity plate embedded in a topographic homogeneous half-space.

than the traditional surface TEM method; however, due to the limitation of observation conditions, the number of receiving devices in the well is limited, affecting the lateral resolution. To analyze the transverse resolution of EM fields, we design four boreholes, located, respectively, at 300, 200, 100, and 0 m from the center of the anomalous body. Among them, the borehole at x = -300 m passes through the center of the inclined plate. Figure 14 shows the relative anomalies calculated from the abnormal responses and background ones in the borehole. Figure 14a shows that since the zero band of Ex moves downward quickly, the Ex component at a depth less than 1000 m is not affected by the zero band at t = 10 ms. Comparing Figures14a and 14b, and the relative anomalies in Figure 14c, the Ex component can better distinguish the location of the inclined plate, but the lateral resolution is limited. There is almost no difference between the background and abnormal responses from the borehole at x = 0, which is far from the abnormal body. In practice, the measurement of Ex and Ey components is still difficult to achieve due to
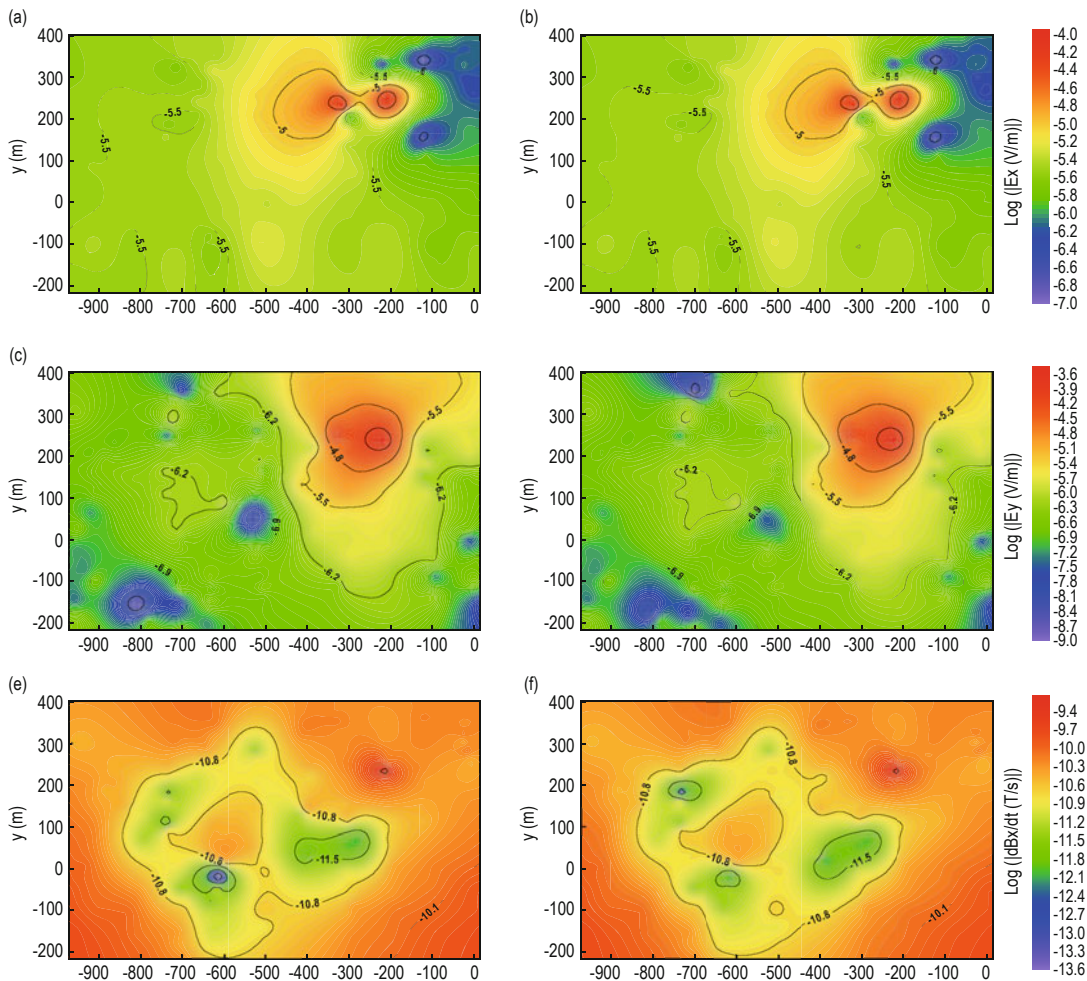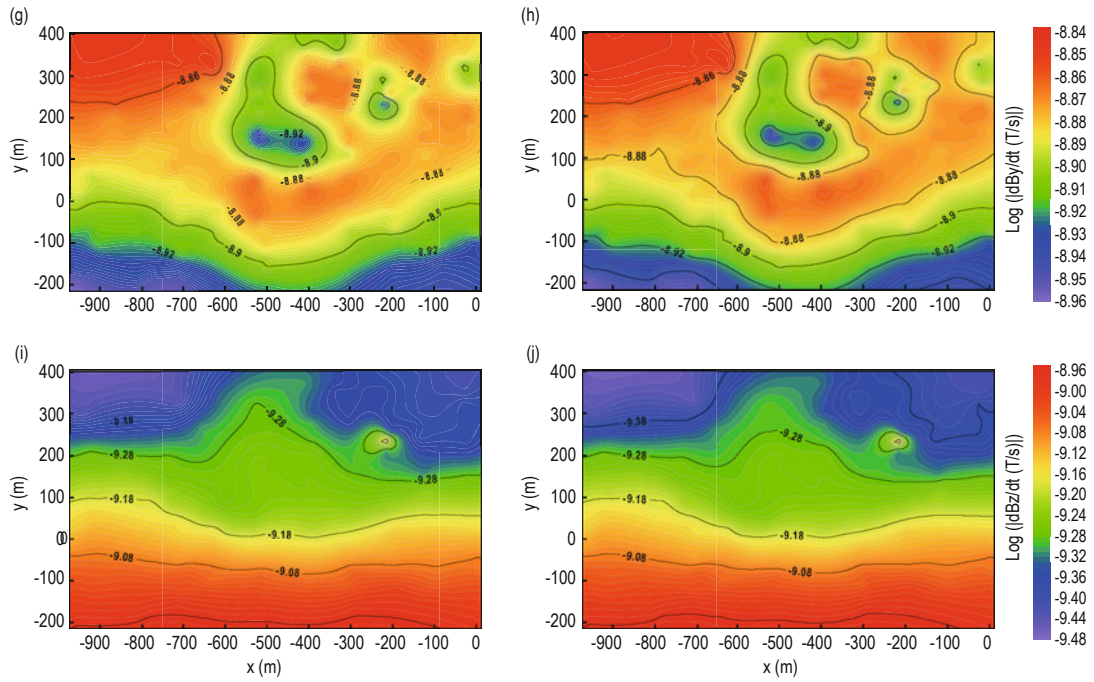
Fig. 13. Comparison of model response to the background response (t = 10ms).
(a)–(b) Ex, (c)–(d) Ez, (e)–(f) dBx/dt, (g)–(h) dBy/dt, (i)–(j) dBz/dt. (a), (c), (e), (g), and (i) show EM responses for the plate model;
(b), (d), (f), (h), and (j) show the background responses without anomalous body.

the small diameter of the borehole. Figures 14d–14f show the curves of the Ez component. The figures show that Ez is highly sensitive to the abnormal body, with the response curves changing rapidly. However, due to the influence of Ez = 0 near the central line of the transmitting source, the shape of the curves is complex.
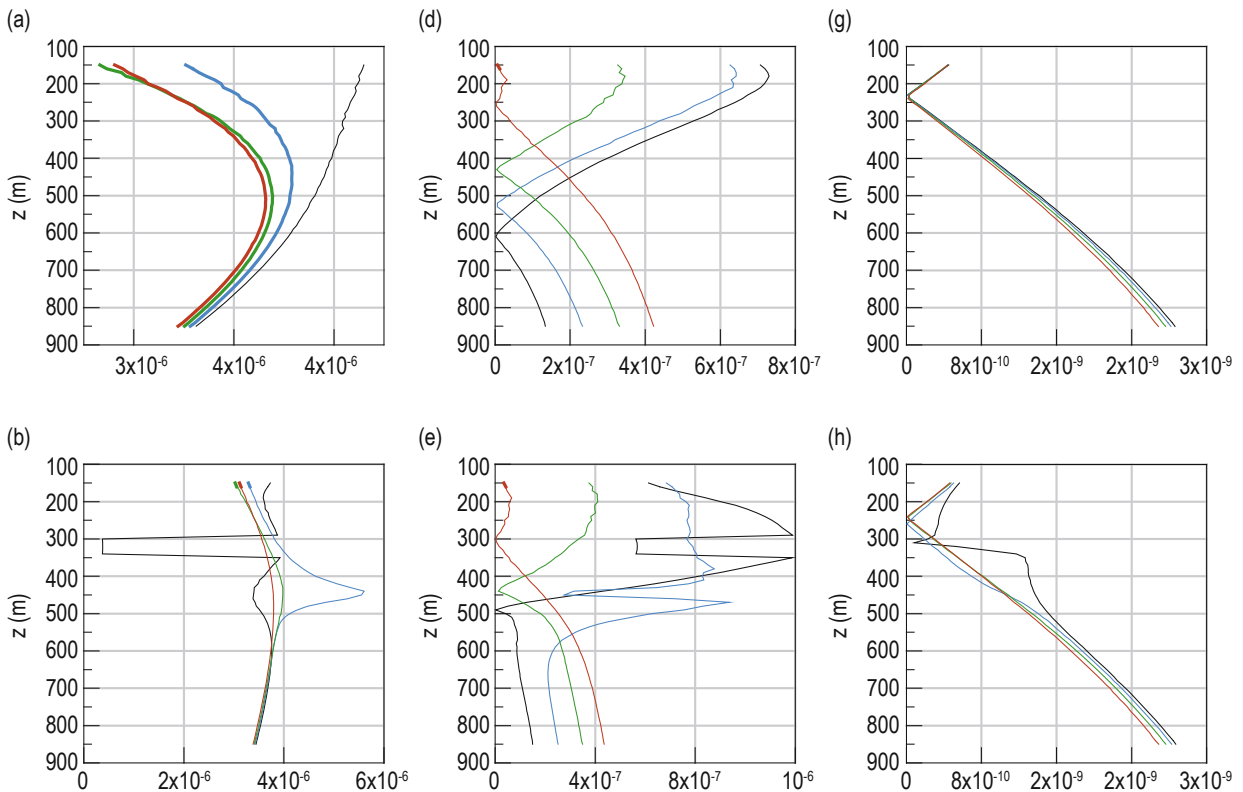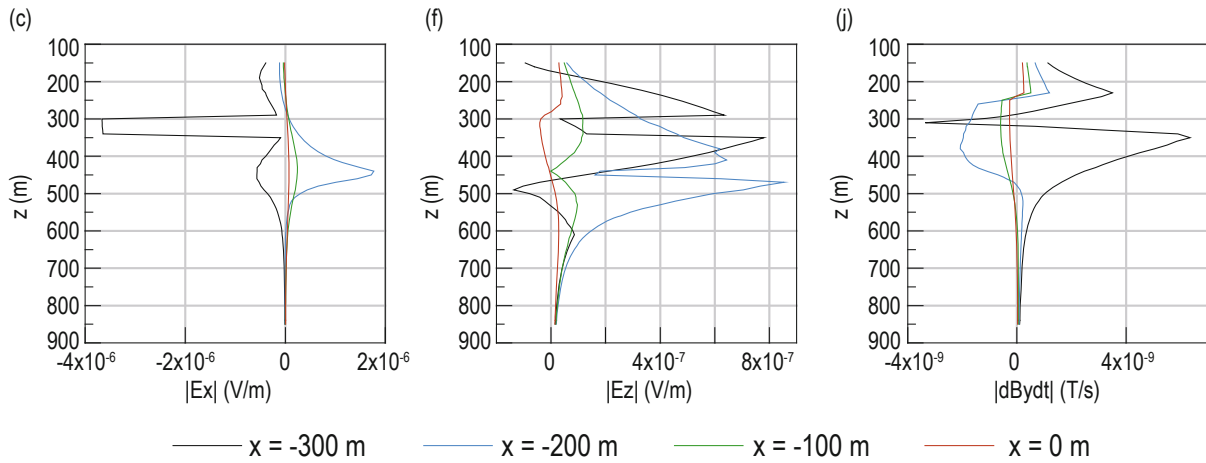
Fig. 14. Responses and relative anomalies for inclined plate model in Figure 12 (t = 10 ms).
(a)–(c) Ex, (d)–(f) Ez, (g)–(i) dBy/dt. (a), (d), and (g) are the background responses; (b), (e), and (h) are the responses for the
inclined plate; (c), (f), and (i) are relative anomalies.

Figures 14g–14i show the curves for dBy/dt responses. Comparing Figures 14i, 14c, and 14f, dBy/dt can more accurately describe the bottom of the inclined plate (at z = 435 m). This demonstrates that dBy/dt has better detection capability in the depth range that is unaffected by the zero band.

Conclusions

Based on the unstructured FE method, we have accomplished 3D numerical simulation for the SBTEM method. Accuracy comparison results of our modeling algorithm and the semi-analytical solution for a homogeneous half-space model confirmed that the proposed algorithm has high accuracy. After simulating and analyzing the characteristics of EM responses for homogeneous half-space and 3D abnormal body models, the diffusion characteristics of EM fields with time are observed, and the generation and distribution of zero bands of EM field components Ex and dBy/dt are determined. This provides the theoretical basis for selecting the most suitable observation borehole to obtain the best target resolution in practice. By analyzing the responses of the inclined plate model under the undulating terrain, we conclude that the SBTEM field is very sensitive to the conductive body, and the SBTEM method can effectively detect a deep underground target. In addition, by comparing the response characteristics of different field components, we found that for an electrical transmitting source, Ez and dBy/dt components have a higher resolution to the conductive abnormal body. We hope that the algorithm presented in this study can promote the development of SBTEM technology in China for deep resource detection.

Acknowledgment

References

Ansari, S., and Farquharson, C.G., 2014, 3D finite-element forward modeling of electromagnetic data using vector and scalar potentials and unstructured grids: Geophysics , **79**(4), E149−E165.

Augustin, A.M., Kennedy, W.D., Morrison, H.F., et al. 1989, A theoretical study of surface−to−borehole electromagnetic logging in cased holes: Geophysics, **54**(1), 90−99.

Buselli, G., and Lee, S.K., 1996, Modelling of drill-hole TEM responses from multiple targets covered by a conductive overburden:. Explor. Geophys. **27**(3), 141−153.

Chen, W.Y., Han, S.X., and Xue, G.Q., 2019, Analysis on the full-component response and detectability of electric source surface-to-borehole TEM method (in Chinese): Chin. J. Geophys. **62**(5), 1969−1980.

Colombo, D. and McNeice, G., 2013, Quantifying

surface-to-reservoir electromagnetics for waterflood monitoring in a Saudi Arabian carbonate reservoir. Geophysics, **78**(6), E281−E290.

Cuevas, N., Colombo, D., Mcneice, G. W., and Pezzli, M., 2015, Field testing and characterization of a transmitter-receiver system for surface to borehole electromagnetic surveys: 77th EAGE Conference & Exhibition, IFEMA Madrid, Spain, June 1−4.

Di, Q.Y., Zhu, R.X., Xue, G.Q., et al., 2019, New development of the Electromagnetic (EM) methods for deep exploration (in Chinese). Chin. J. Geophys., **62**(6), 2128−2138.

Dyck, A.V., and West, G.F. 1984, The role of simple computer models in interpretations of wide-band, drillhole electromagnetic surveys in mineral exploration: Geophysics, **49**(7), 957−980.

Eaton, P.A., Hohmann, G.W., 1984, The influence of a conductive host on two-dimensional borehole transient electromagnetic responses. Geophysics, **49**(7), 861−869.

Gunderson, B.M., Newman, G.A., and Hohmann, G.W., 1986, Three-dimensional transient electromagnetic responses for a grounded source. Geophysics, **51**(11), 2117−2130.

Haroon, A., Adrian, J., Bergers, R., et al., 2015, Joint inversion of long-offset and central-loop transient electromagnetic data: Application to a mud volcano exploration in Perekishkul, Azerbaijan. Geophys. Prospect. **63**(2), 478−494.

Hui, Z.J., Yin, C.C., Liu, Y.H., et al., 2020, 3D inversions of time-domain marine EM data based on unstructured finite-element method (in Chinese): Chin. J. Geophys. **63**(8), 3167−3179.

Jin, J.M., 1998, The finite element method in electromagnetics: Xidian University Press, China, 150−152.

Li, J.H., 2015, Inversion algorithms for electromagnetic problems in well: numerical examples in reservoir target detection:. PhD Thesis, China University of Geosciences, Wuhan.

Li, J.H., Liu, S.C., Jiao, X.F., et al., 2015, Three-dimensional forward modeling for surface borehole transient electromagnetic method (in Chinese): Oil Geophysical Prospecting, **20**(3), 556−564.

Li, J.H., and He, Z.X., 2012, 3D electrical response characteristics modeling for surface-to-borehole vertical electromagnetic walkaway profile (in Chinese): Oil Geophysical Prospecting **47**(4), 653−664.

Li, J.H., He, Z.X., and Xu, Y.X., 2017, Three-dimensional numerical modeling of surface-to-

borehole electromagnetic method for monitoring reservoir: Applied Geophysics **14**(4), 1672−7975.

Liu, C., Li, Z.H., and Abbassi, B., 2020, 3D parallel surface-borehole TEM forward modeling with multiple meshes. J. Appl. Geophy. **172**, 103916.

Macnae, J., and Staltari, G., 1987, Classification of sign changes in borehole TEM decays: Explor. Geophys. **18**(3), 331−339.

Meier, P., Kalscheuer, T., Podgorski, J.E., et al., 2014, Hydrogeophysical investigations in the western and north-central okavango delta (botswana) based on helicopter and ground-based transient electromagnetic data and electrical resistance tomography: Geophysics, **79**(5), B201−B211.

Meng, Q.X., and Pan, H.P., 2012, Numerical simulation analysis of surface-hole TEM responses (in Chinese): Chin. J. Geophys., **55**(3),1046−1053.

Newman, G.A., Anderson, W.L., and Hohmann, G.W., 1989, Effect of conductive host rock on borehole transient electromagnetic responses. Geophysics **54**(5), 598−608.

Oldenburg, D.W., Haber, E., and Shekhtman, R., 2013, Three dimensional inversion of multisource time domain electromagnetic data: Geophysics, **78**(1), E47−E57.

Porsani, J.L., Bortolozo, C.A., Almeida, E.R., et al., 2012, TDEM survey in urban environmental for hydrogeological study at USP campus in So Paulo city, Brazil: J. Appl. Geophy. **76**, 102−108.

Si, H., 2007, TetGen: A Quality Tetrahedral Mesh Generator and 3D Delaunay Triangulator.

Spies, B.R., and Greavesb, R.J., 1991, Numerical modeling of surface-to-borehole electromagnetic surveys for monitoring thermal enhanced oil recovery: Geoexploration, **28**(3−4), 293−311.

Strack, K.-M., Lüschen, E., and Kötz, A., 1990, Long-offset transient electromagnetic (LOTEM) depth soundings applied to crustal studies in the Black Forest and Swabian Alb, Federal Republic of Germany: Geophysics **55**(7), 834−842.

Swidinsky, A., Hölz, S., and Jegen, M., 2012, On mapping seafloor mineral deposits with central loop transient electromagnetics: Geophysics, **77**(3), E171−184.

Um, E.S., 2011, Three-Dimension finite-element time-domain modeling of the marine controlled-source electromagnetic method: PhD Thesis, Stanford University, Stanford.

Um, E.S., Harris, J.M., and Alumbaugh, D.L., 2010, 3D time-domain simulation of electromagnetic diffusion phenomena: a finite-element electric-field approach:

Geophysics **75**(4), F115−F126.

West, R.C., and Ward, S.H., 1988, The borehole transient electromagnetic response of a three-dimensional fracture zone in a conductive half-space: Geophysics **53**(11), 1469−1478.
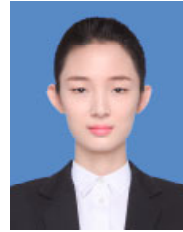
Xue, G.Q., Chen, W.Y., Zhou, N.N., and Li, H., 2013, Short-offset TEM technique with a grounded wire source for deep sounding (in Chinese). Chin. J. Geophys. **1**, 225−261.

Yang, H.Y., Xu, Z.Y., Yue, J.H., et al., 2016, 3D inclined conductor behavior of down-hole transient electromagnetic method with overburden layer (in Chinese): Geophysical & Geochemical Exploration, **40**(1), 190−196.

Yin, C.C., Qi, Y.F., Liu, Y.H., and Cai, J., 2016, 3D time-domain airborne EM forward modeling with topography: J. Appl. Geophy. **134**, 11−22.

Wang Lu-Yuan, a graduate student, received her bachelor's degree from the College of Geo-Exploration Science and Technology of Jilin University in 2019 and is currently pursuing a master's degree from the College of Geo-Exploration Science and Technology of Jilin University. She is primarily engaged in geophysical electromagnetic forward and inversion theory.

E-mail: Wangly2315@163.com